

Earth and Space Science



RESEARCH ARTICLE

10.1029/2024EA003909

Key Points:

- A 3-axis quartz crystal accelerometer is calibrated against gravity to remove drift from measurements of tilt in the horizontal channels
- Calibrations for separate field tests in a vault and on the seafloor are fit by a linear-exponential drift model to $\sim 1 \mu\text{g}$ residual
- Calibrations suggest variable span changes by sensor, from approximately 1–5 $\mu\text{g}/\text{yr}$, or 1%–22% of the respective drift rate

Supporting Information:

Supporting Information may be found in the online version of this article.

Correspondence to:

E. K. Fredrickson,
erikfred@utexas.edu

Citation:

Fredrickson, E. K., Wilcock, W. S. D., Harrington, M. J., Cram, G., Tilley, J., Martin, D., & Burnett, J. (2024). The self-calibrating tilt accelerometer: A method for observing tilt and correcting drift with a triaxial accelerometer. *Earth and Space Science*, 11, e2024EA003909. <https://doi.org/10.1029/2024EA003909>

Received 5 AUG 2024

Accepted 5 OCT 2024

Author Contributions:

Conceptualization: W. S. D. Wilcock, M. J. Harrington, G. Cram

Data curation: E. K. Fredrickson, M. J. Harrington

Formal analysis: E. K. Fredrickson

Funding acquisition: W. S. D. Wilcock

Investigation: E. K. Fredrickson

Methodology: E. K. Fredrickson, W. S. D. Wilcock, M. J. Harrington, G. Cram

Project administration:

W. S. D. Wilcock

Resources: M. J. Harrington, G. Cram,

J. Tilley, D. Martin, J. Burnett

Supervision: W. S. D. Wilcock

© 2024. The Author(s).

This is an open access article under the terms of the [Creative Commons Attribution License](#), which permits use, distribution and reproduction in any medium, provided the original work is properly cited.

The Self-Calibrating Tilt Accelerometer: A Method for Observing Tilt and Correcting Drift With a Triaxial Accelerometer

E. K. Fredrickson¹ , W. S. D. Wilcock², M. J. Harrington³, G. Cram³, J. Tilley³, D. Martin³, and J. Burnett³

¹University of Texas at Austin, Institute for Geophysics, Austin, TX, USA, ²School of Oceanography, University of Washington, Seattle, WA, USA, ³Applied Physics Laboratory, University of Washington, Seattle, WA, USA

Abstract We present observations from two field deployments of a calibrated tiltmeter that we name the Self-Calibrating Tilt Accelerometer (SCTA). The tiltmeter is based upon a triaxial quartz crystal accelerometer; the horizontal channels measure tilt and are periodically rotated into the vertical to obtain a measurement of the acceleration of gravity. Changes in the measured total acceleration are ascribed to drift in the vertical channel and used as calibrations for removing that same drift from the tilt time series observed between calibrations. Changes in the span (sensitivity) of the accelerometer channels can also be measured by calibrating them pointing up and down. A 3-year test on the seafloor at Axial Seamount show that the calibrations are consistent with a linear-exponential model of drift to a RMS residual of $\sim 0.5 \mu\text{g}$ (μrad). The calibrated tilt time series was impacted by platform settling for the first 2 years, but after repositioning the tiltmeter, the calibrated observations were consistent for the final year with the tilt observed on a nearby LILY tiltmeter, within an assumed level of drift for the unconstrained LILY sensor. A separate 15-month test in a stable vault at Piñon Flat Observatory was complicated by seasonal temperature variations of $>5^\circ\text{C}$; the calibrations are consistent with a linear-exponential model of drift to $\sim 2 \mu\text{g}$ RMS when temperature and temperature time-derivative dependence is included. Similarly, the calibrated tilt time series was impacted by thermal deformation of the SCTA assembly. A future test in a thermally and tectonically stable borehole will be required to assess the accuracy of the SCTA.

Plain Language Summary We developed a new instrument for measuring the tilt of a surface to a high degree of accuracy, on the order of a millionth of a radian. This instrument, the Self-Calibrating Tilt Accelerometer (SCTA), combines three sensor channels that measure acceleration, arranged so that two channels are horizontal at right angles and the other is vertical. Tilting of the ground surface moves the horizontal channels toward alignment with the (vertical) gravitational acceleration, producing an observable signal. The SCTA can rotate to put any of the three channels into the vertical, where they can be calibrated against the full, effectively constant gravitational acceleration. These calibrations correct the horizontal tilt measurements for artificial signals generated within the sensors, yielding reliable measurements of the tilt of the ground surface. We present data from two deployments of the SCTA concept, one land-based at Piñon Flats Observatory and the other seafloor-based at Axial Seamount. At Axial, there is ongoing tilting of the seafloor from volcanic inflation that the SCTA measures consistent with a nearby, independent sensor. Piñon Flats should be tectonically stable, but seasonal temperature fluctuations at the site induced apparent tilt signals from internal deformation of the SCTA assembly.

1. Introduction

Geodetic measurements complement seismic observations, because together they provide a comprehensive view of tectonic processes (e.g., Bevis et al., 2001; Bock et al., 1993; Feigl et al., 1993; Kreemer et al., 2014; Massonnet et al., 1993; McCaffrey et al., 2013). On land, spaced-based Global Navigation Satellite System (GNSS) and Interferometric Synthetic Aperture Radar (InSAR) geodetic techniques have revolutionized studies of plate boundary and volcanic deformation by providing observations with spatial and temporal resolutions unattainable with other approaches (Burgman & Thatcher, 2013; Poland & Zebker, 2022). However, this revolution does not extend to the seafloor because the oceans do not transmit the electromagnetic waves on which the spaced-based techniques are based. Thus, the challenge of seafloor geodesy provides impetus for continued development of

Writing – original draft:

E. K. Fredrickson

Writing – review & editing:

W. S. D. Wilcock

traditional geodetic measurements that are presently of relatively minor importance on land (Bürgmann & Chadwell, 2014).

One long-established geodetic measurement is tilt, the change in attitude of a surface, which is more sensitive to deformation than elevation observations such as GNSS and InSAR (e.g., Davis et al., 2023). There are two broad classes of tiltmeters: long baseline and short baseline (Agnew & Wyatt, 1989). Long baseline units measure the relative change in elevation of two connected liquid surfaces up to hundreds of meters apart. Short baseline units measure change in the tilt of a small platform, either by sensing the movement of a bubble in a fluid trapped beneath a convex surface (e.g., Kimura et al., 2013) or by measuring the deflection of a vertical pendulum (e.g., Zumberge et al., 2018). Highly compact micro-electromechanical system (MEMS) tiltmeters, such as those used in modern electronics, are becoming increasingly sensitive but tend to have large or entirely unconstrained drift characteristics (e.g., Liu et al., 2022). By nature of their size, long baseline tiltmeters are relatively unsusceptible to hyper-local effects like platform settling and small block motion, making them suitable for observations of secular strain. They have high resolution and can achieve low drift rates on the order of 1 $\mu\text{rad}/\text{yr}$ (Wyatt, 1982). However, there are many applications in which long-baseline instruments are impractical because of their cost, size, and installation needs, such as for rapid response, difficult-to-access locations, and settings where many sensors are required to resolve complex deformation. On the seafloor, only one long-baseline tiltmeter has been deployed (Anderson et al., 1997). Over 2 months in 1994, an installation at Axial Seamount measured variable long-period signals of several $\mu\text{rad}/\text{day}$ that could not be categorized between endpoint settling, instrumental drift, and volcanic inflation. While the authors identified approaches to improve the stability of future deployments, no further experiments were attempted.

Short baseline tiltmeters are easier to deploy but the less expensive bubble tiltmeters experience significant instrumental drift of 10–100 $\mu\text{rad}/\text{yr}$ that is unique to each individual instrument and can vary significantly over the deployment interval. They are most frequently deployed to monitor rapidly deforming volcanoes, where geophysical signals can surpass drift and thermal effects (e.g., Dvorak & Dzurisin, 1997). High-resolution tiltmeters with lower inherent drift rates have also been developed for borehole applications (Chawah et al., 2015; Jahr et al., 2006) but the technology is expensive, and drift can result from temperature dependence and the mechanical leveling systems needed for instruments with a small dynamic range. Additional concepts for short-baseline sensors continue to be developed, such as models that utilize optical interferometry (e.g., Esmaeili et al., 2023; Zumberge et al., 2018) or traditional pendulums (e.g., Gravirov et al., 2022), but drift and thermal sensitivity remain pervasive problems. Statistical techniques exist to isolate drift from physical tilt signals, but they require initially low drift rates on the order of a few $\mu\text{rad}/\text{yr}$ (Furst et al., 2019).

Significant efforts have been made to develop short baseline tiltmeters for the seafloor (Anderson et al., 1997; Fabian & Villinger, 2007; Hensch et al., 2009; Sakata & Shimada, 1984; Shimamura & Kanazawa, 1988; Shiobara et al., 2021; Takamori et al., 2011; Tolstoy et al., 1998) and such sensors have detected short-term geological signals. In a single-tiltmeter experiment in the Logachev hydrothermal field, Fabian and Villinger (2008) recorded large changes in tilt of up to 10,000 μrads over the 1 year observation period, possibly resulting from earthquakes and nearby mass wasting. Cabled tiltmeters on the Ocean Observatories Initiative (OOI) Regional Cabled Array (RCA) measured signals of hundreds of μrads during the 2015 eruption of Axial Seamount that constrained the timing and direction of dike propagation (Nooner & Chadwick, 2016). Shiobara et al. (2021) observed tilt signals of up to a few tens of μrads associated with shallow slow-slip events offshore Japan. However, as on land, drift limits the capabilities to measure longer term signals. Because of drift, short-baseline tiltmeters are often considered reliable only for measuring short-period and/or large-amplitude signals, despite the nanoradian resolution of modern sensors (Jahr et al., 2009). For example, Tolstoy et al. (1998) found at the end of a 2-month deployment at Axial Seamount, the combined drift and settling rates of four short period tiltmeters were $\sim 1 \mu\text{rad}/\text{day}$, sufficiently low to detect volcanic events but not to measure inflation. Likewise, the longer-term volcano inflation tilt signals on the OOI RCA tiltmeters have proved challenging to interpret (Fredrickson et al., 2019), possibly because of instrumental drift.

Several short baseline tiltmeters have also been developed for seafloor boreholes (Duennebier et al., 1987; Kitada et al., 2013; McGuire et al., 2018; Party, 2000; Tsuji et al., 2023). A tiltmeter is included in the geophysical packages deployed in the NanTroSEIZE boreholes in Nankai Trough subduction zone offshore Japan (Kitada et al., 2013), but did not detect signals from the 2016 small slow slip events that were observed with formation pressure measurements (Araki et al., 2017). In 2016 a tiltmeter was installed in hole U1364A in the Cascadia

subduction zone, but the available data have shown no evidence that slow slip events were triggered by the dynamic stress from teleseismic earthquakes (McGuire et al., 2018). Again in Nankai Trough, Tsuji et al. (2023) report on a LILY bubble level tiltmeter installed in 2019 in an 8.6 m borehole and an optical tiltmeter developed by Zumberge et al. (2018) installed in 2021 in a 20 m borehole. Neither have recorded evidence of slow slip, but the authors noted that the superior noise characteristics of the optical sensor should enable it to record future events.

The experiences from past deployments of short baseline tiltmeter provide clear motivation for continued development of approaches to detect small transient and secular signals. Here, we present a new approach to reducing the drift in tilt measured by the horizontal channels of a three-component, high-resolution quartz crystal accelerometer by periodically rotating the horizontal channels into the vertical to calibrate against local gravity (g). We describe our instrument, the Self-Calibrating Tilt Accelerometer (SCTA), and evaluate its capabilities with two deployments: one on the seafloor on a submarine volcano and the other on land in a vault at a geophysical observatory.

2. Materials and Methods

2.1. Calibration Principle

The SCTA uses a Quartz Seismic Sensors, Inc. triaxial accelerometer with a full scale of $\pm 3g$ and a resolution of parts per billion. The accelerometer works by measuring changes in the oscillation frequency of three isolated quartz crystal resonators as they are strained by accelerations in orthogonal directions. The oscillation frequency of a fourth unstrained quartz resonator measures temperature and is used to provide temperature corrections to the frequency outputs of the accelerometers. Although quartz crystal resonators are remarkably sensitive to changes in load, they are well known to undergo significant instrumental drift (Polster et al., 2009; Watts & Kon-toyiannis, 1990). This drift is often characterized by a combination of linear and exponential functions, but the amplitudes and time constants vary between sensors and between deployments of the same sensor, so cannot be predicted. In the absence of other signals, the accelerometer's three channels measure g . A factory calibration internally corrects the outputs of the three accelerometers for small orientation offsets from orthogonality so that the scalar value of g is independent of orientation.

To avoid ambiguity, we will refer to the SCTA's three accelerometer channels as capital X , Y , and Z , and refer to coordinate system axes as lowercase x , y , and z , with x and y in the horizontal plane and z vertical up. When X and Y are nearly horizontal and Z , thus, nearly vertical—the measurement orientation shown in Figure 1a—the horizontal channels will measure accelerations

$$a_X(t) = g \sin \theta_X(t) + \sigma_X(t) \approx g \theta_X(t) + \sigma_X(t) \quad (1)$$

$$a_Y(t) = g \sin \theta_Y(t) + \sigma_Y(t) \approx g \theta_Y(t) + \sigma_Y(t)$$

where θ_X is the angle between X and x , θ_Y is the angle between Y and y , σ_X and σ_Y are the drift for each channel, and t is time. For small tilts, these accelerations are linearly dependent on tilt but are also sensitive to drift. Conversely, the channel in the vertical measures

$$a_Z(t) = g \cos \theta_Z(t) + \sigma_Z(t) \quad (2)$$

where θ_Z is the angle between Z and z . For small tilts, this acceleration is largely insensitive to tilt but is subject to drift. The total acceleration, a_T can be written from the three orthogonal accelerations as

$$a_T(t) = \sqrt{a_X^2 + a_Y^2 + a_Z^2} \approx g \cos \theta_Z(t) + \sigma_Z(t) \approx g + \sigma_Z(t) \quad (3)$$

Provided the Z channel is within a few degrees of vertical, the acceleration it measures will, to a good approximation, be the sum of the magnitude of g and the accumulated drift of the vertical channel since the factory calibration.

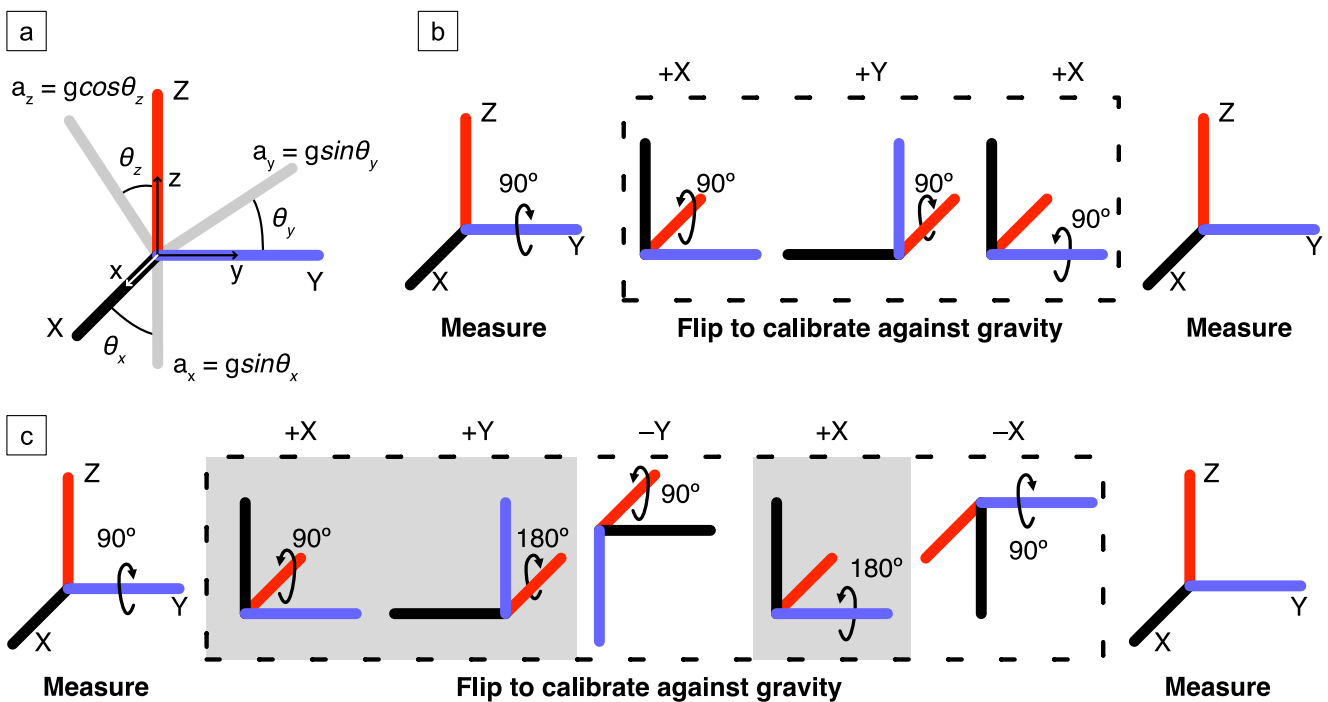


Figure 1. (a) Notation used to indicate accelerometer orientations when making tilt measurements (b) Schematic of the 3-orientation rotation sequence used during calibrations prior to 9 August 2021. The colors correspond to the same axes throughout the sequence. Arrows indicate the sense of rotation applied to get to the next orientation. (c) As in (b), but for the 5-orientation rotation sequence used for all calibrations on and after 9 August 2021. Gray shading indicates the orientations common to the sequence shown in (b).

If a horizontal channel is temporarily rotated into the vertical at the start and end of a measurement interval, then the change in the total accelerations between the two rotations will, following Equation 3, be a measure of the drift of that channel, s , over the measurement interval, provided g is constant. This can be expressed for the two horizontal channels

$$\begin{aligned} a_T^X(t_k) &= g + \sigma_X(t_k) \\ a_T^Y(t_k) &= g + \sigma_Y(t_k) \end{aligned} \quad (4)$$

where the superscripts X and Y indicate the channel rotated into the vertical and t_k is the time of the k th calibration. This drift is measured in the vertical orientation but can be applied to measurements in the horizontal under the assumption that the drift is independent of orientation, that is, that the measurement span of the accelerometer does not change with time.

Considering just one measurement interval, the difference between the start and end calibrations can be used to apply a linear drift correction. Since it is impractical to return the horizontal channels to precisely the same orientation after a calibration, static offsets will result after a calibration, and it is necessary to stitch together the measurement segments between multiple calibrations. This can be done by applying simple offsets to linearly corrected segments but also provides an opportunity to fit a more complex linear plus exponential drift model and account for residual temperature sensitivity.

2.2. SCTA Design

The accelerometer casing is a 6.32-cm-long cylinder of radius 1.5 cm, with the Z axis along the axis of the cylinder and the X and Y axes perpendicular to the cylinder axis in a right-handed configuration. The SCTA houses the accelerometer within a two-axis gimbal system that normally holds the Z channel vertical (Figures 2a–2c). The axis of the inner gimbal is parallel to the Z channel and that of the outer gimbal parallel to the X channel. The outer gimbal is used to rotate the Z channel into the horizontal while the rotation of the inner gimbal controls whether

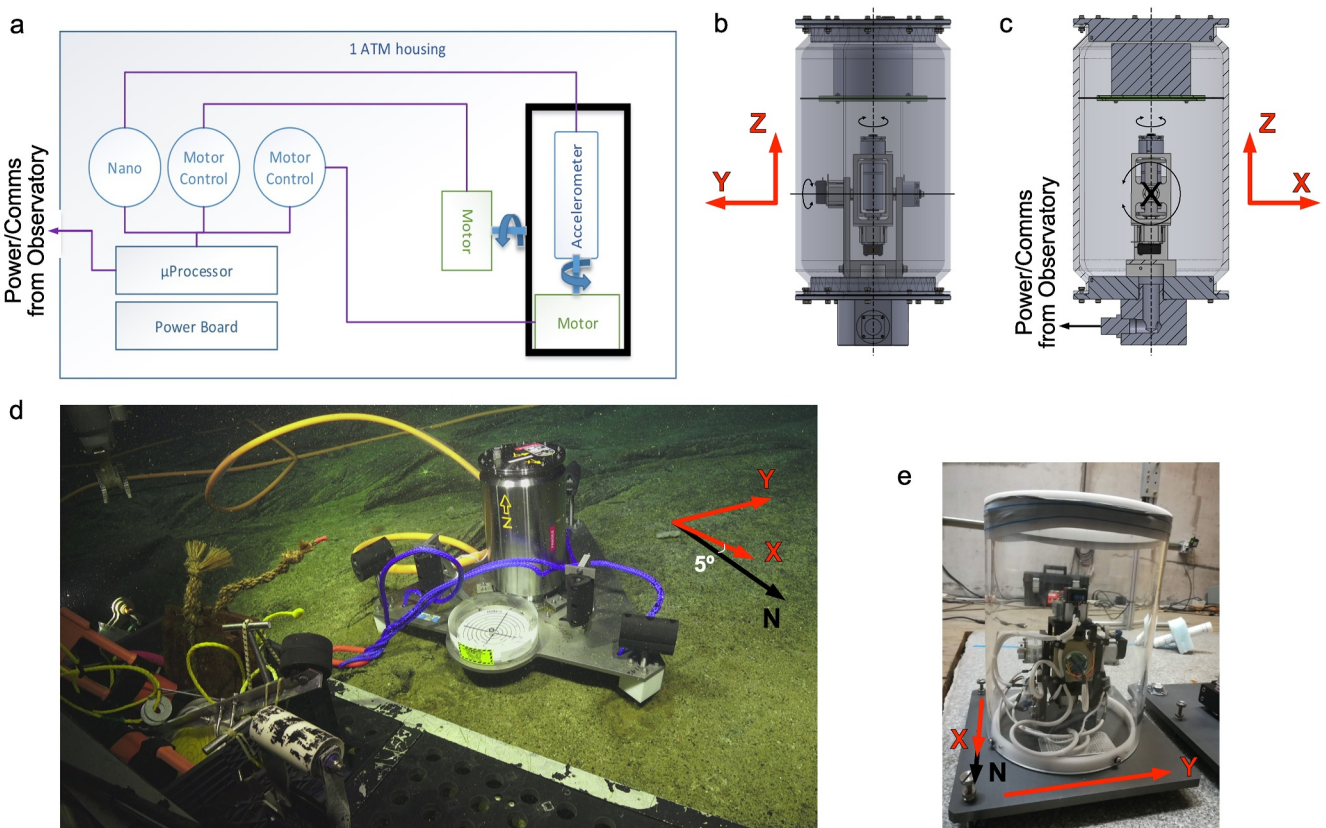


Figure 2. (a) Conceptual diagram of SCTA design showing the stepping motors that rotate the accelerometer, the motor control, Paroscientific Nano-Resolution frequency counting, the microprocessor and power boards. (b) Schematic of SCTA housing and gimbal design, with accelerometer shown in the center. The vertical dashed line indicates the axis of rotation for the inner gimbal and the horizontal solid line indicates the axis of rotation for the outer gimbal. The orientation of the Z and Y channels with respect to the gimbals is shown at left, with X pointing into the page. (c) Side-view schematic of the SCTA housing and gimbal design. The vertical dashed line indicates the axis of rotation for the inner gimbal and the black “x” indicates the axis of rotation for the outer gimbal. The orientation of the Z and X channels is shown at right, with Y pointing into the page. (d) Axial Seamount SCTA on the seafloor at Location 1 showing the orientation of the X and Y channels (X at an azimuth of 355°). The leg that we inferred to be subsiding is on the left. At Location 2, the X channel was at an azimuth of 340°. (e) Piñon Flat SCTA in the vault showing the channel orientations (X is due north).

the X channel or Y channel is vertical. The rotations are driven by stepper motors from Lin Engineering and an encoder from U.S. Digital that together give an effective step increment of 0.072°. The accelerometer is held in place between rotations by electromagnetic brakes from Stock Drive Products. Heat generation is minimized by powering off the motors between calibrations and setting the brakes to power-off engage.

In our testing we employed two rotational sequences (Figure 1). The first comprises a 90° rotation of the outer gimbal, a 90° rotation of the inner gimbal, and then a reversal of the rotations of the inner and outer gimbals (Figure 1b). This results in a three-orientation calibration sequence in which +X, +Y, and +X are sequentially moved into the vertical for calibrations before the accelerometer returns to the measurement orientation. The second rotational sequence is a five-orientation sequence in which +X, +Y, -Y, +X, and -X, are sequentially rotated into the vertical before returning to the measurement orientation (Figure 1c). This more complex sequence enables a calibration of the accelerometer span by measuring acceleration with each horizontal channel pointing both up and down. Because changes in the accelerometer orientation lead to repeatable short-term transients in the accelerometer output, it is important to maintain a consistent timing for the calibration sequences. For both sequences, the gimbals were rotated at 90° per 10 s and the accelerometer was held in each orientation for 110 s. The ordering is imposed by the geometry of the SCTA’s internal wiring which limits the rotations of each gimbal to ±90°. This geometrical constraint also led both sequences to include two calibrations in the +X orientation, which we term +X1 and +X2, and serve as a check on consistency.

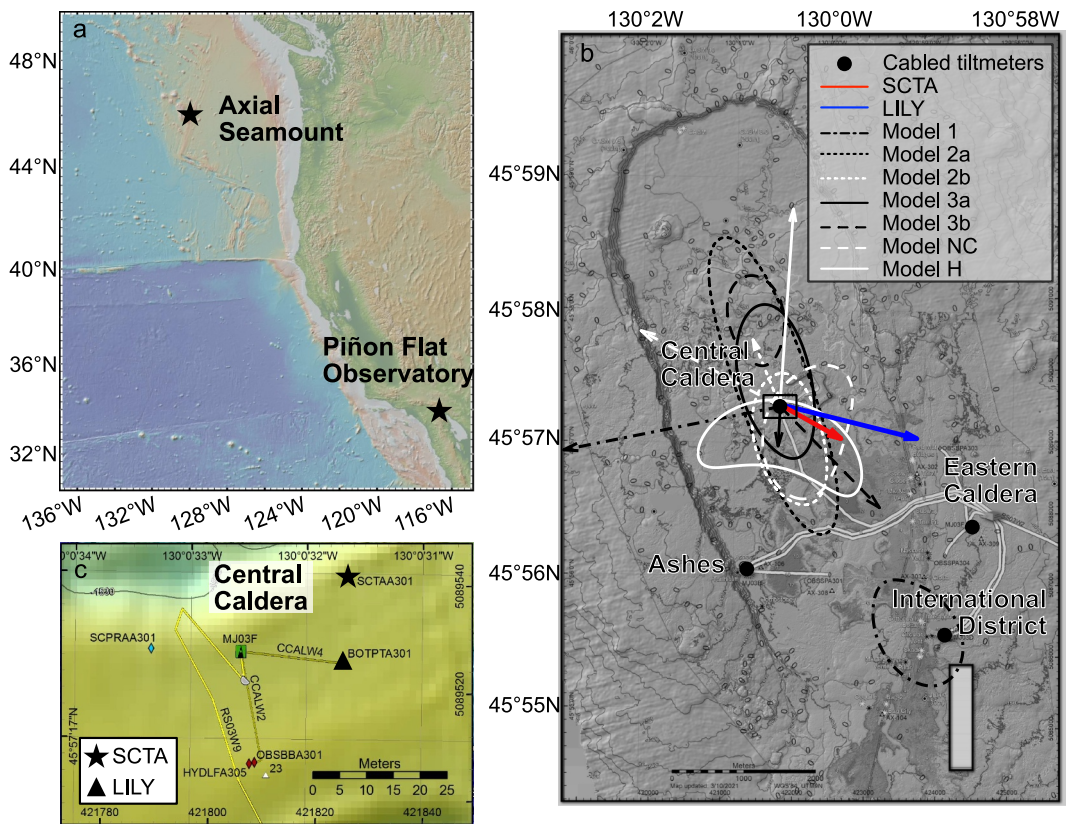


Figure 3. (a) Map showing the location of Axial Seamount and Piñon Flat Observatory (PFO). (b) Bathymetric map of the Axial Seamount summit caldera (courtesy of Deborah Kelley). The square box around the Central Caldera site shows the area of (c). The four black circles show the OOI RCA cabled tiltmeter sites and the cables are shown in white for the trunk line to the primary node and in yellow for cables to secondary infrastructure. The red and blue vectors show the inferred tilt directions from the SCTA and LILY tiltmeter, respectively, over the period of this study. They are scaled proportionally to one another, but otherwise at arbitrary scale. The black and white ellipsoids contour 95% of maximum inflation from various modeling efforts, while the vectors of the same shade and pattern show the corresponding tilt predictions. Again, the model vectors are scaled relative to one another but otherwise at arbitrary scale. “Model 1,” “Model 2a,” “Model 2b,” “Model 3a,” and “Model 3b” are from Slead et al. (2024), wherein they have the same names. “Model NC” is from Nooner and Chadwick (2016) and “Model H” is from Hefner et al. (2020). Refer to the main text for further descriptions of these models. Note that the tilt predicted by Model 2a is an order of magnitude smaller than that of the other models and its vector is not visible as a result. (c) Zoom map of the OOI RCA infrastructure at the Central Caldera site (courtesy of the OOI RCA) showing the deployment locations of the SCTA and LILY tiltmeter.

3. Field Tests

3.1. Axial Seamount

On 6 July 2018, the seafloor version of the SCTA was connected to the OOI RCA cabled observatory at the central caldera site of Axial Seamount at 45.955°N , 130.008°W (Figures 2c, 3a and 3b) using a remotely operated vehicle (ROV). Axial Seamount is an active undersea volcano on the Juan de Fuca Ridge and the current eruptive edifice for the Cobb Hotspot. The summit of the seamount is characterized by a 100-m-deep, 8-km-by-3-km horseshoe-shaped caldera whose wall demarks an inward-dipping ring fault that meets a conjugate outward-dipping fault at 0.5–1 km depth (Wilcock et al., 2016). The volcanic system is characterized by a 14 km by 3 km central magma chamber at 1.1–2.3 km depth, with up to 1 km thickness (Arnulf et al., 2014). The main magma body is surrounded by several other shallow magma bodies, including a recently discovered reservoir to the west of the central magma chamber, all of which have been constrained to maximum melt fractions of 10%–32% (Yang et al., 2024). These features are underlain by a 3–5 km diameter region of stacked reflectors extending to 5 km depth that are interpreted to be a series of melt sills within a column of mush that feeds the upper crustal magma chamber (Carbotte et al., 2020).

Geodetic measurements have been ongoing here since 1987, starting with intermittent deployments of a bottom pressure recorder (Fox, 1993). There is a near continuous time series of calibrated bottom pressure observations that spans the three most recent eruptions in 1998, 2011, and 2015 (Chadwick et al., 2006, 2012; Nooner & Chadwick, 2009, 2016). Each eruption is accompanied by several meters of subsidence and the eruptions occur when the caldera floor has reinflated back to a predictable level (Nooner & Chadwick, 2016). A long-term view of the geodetic record at Axial shows an order of magnitude variation in average inflation rate since continuous observation began in 1998, with the most recent observations showing that the caldera has recovered most of the 2015 deflation (Chadwick et al., 2022). However, the rate of inflation has decelerated notably over the past few years, with sporadic intervals of increased inflation, leading to uncertain and variable forecasts of the next eruption (https://www.pmel.noaa.gov/eo/axial_blog.html). The OOI RCA operates four cabled bottom pressure and tilt sensors that include a Jewell Instruments LILY tiltmeter with a dynamic range of 330 μ rad and a resolution of 5 nrad. One of these instruments is located 20 m from the SCTA deployment site at a heading of 187° (Figure 3c). In summer 2022, four acoustic ranging instruments were deployed on the Axial Caldera to add horizontal geodetic observing capability to the existing network (Kidiwela et al., 2023).

The SCTA at Axial was housed within a titanium cylinder that was oriented vertically and attached to a triangular metal platform with three leveling feet that were adjusted by the ROV to level the housing within 1° (Figure 2d). Data from Axial were initially collected from 06 August 2018 to 10 September 2020 (data streaming and archiving did not start until 10 October 2018). We then moved the SCTA a few meters and resumed data collection from 11 September 2020 to 27 August 2021. The instrument was repositioned because one of the SCTA platform's feet appeared to be settling, with an anomalously large, ongoing tilt signal on the Y channel and evidence of loose sediments after reinspecting video footage taken during the deployment. Settling was supported by observations of sediment erosion around the subsiding foot when the sensor was relocated. We refer to the initial deployment location as "Location 1" and the re-positioned location as "Location 2." Data were streamed to shore at 40 and 8 Hz, and archived in near-real time at the Incorporated Research Institutions for Seismology Data Management Center (IRIS DMC) as station AXCC2 on network OO, with the high-rate data occasionally sequestered by the U.S. Navy (Rutgers, 2013).

At Axial Seamount Location 1, the no data were collected for 27 days of the 689-day deployment, while at Location 2, data are missing for only four of the 350 days. The data gaps resulted from OOI Cabled Array outages and loss of software connectivity to the SCTA. Figure 4 shows representative examples of the observed acceleration and power spectra for the SCTA in its measurement orientation for both Axial Seamount locations. The secondary microseism peak is clearly visible at both locations, for all channels, between 0.1 and 1 Hz. At Location 1, there is a pronounced peak in power at 0.05–0.06 Hz which we attribute to rocking due to the unstable footing (Figure 4b). The horizontal channels are also noisier at frequencies above the microseism for Location 1, which again may be indicative of platform instability. At Location 2, sharp peaks at 2 and 3 Hz and just below 5 Hz may be related to mechanical resonances of the gimbal system. Bottom temperatures at Axial Seamount are stable with the internal temperature of the housing characterized by seasonal variations of 0.15°C (5.60–5.75°C) and a daily standard deviation of <0.05°C.

In total, 125 calibrations of the SCTA were obtained at Axial Seamount. Sixty-five were obtained at Location 1, of which the first 24 (prior to 13 August 2019) were three-orientation sequences and the remaining 41 were 5-orientation sequences (Table S1 in Supporting Information S1), and 60 were obtained at Location 2 (all five-orientation sequences) (Table S2 in Supporting Information S1). The time between calibrations varied from a day to a month, with occasional longer intervals when communication with the SCTA was lost.

3.2. Piñon Flat Observatory

A second SCTA was operated at a terrestrial site, the Scripps Institution of Oceanography's Cecil and Ida Green Piñon Flat Observatory (PFO) at 33.611°N, 116.455°W (Figure 3a). PFO is located at the northern end of the Santa Rosa Mountains, ~30 km southwest of the city of Palm Desert, California. This site has relatively smooth topography (Wyatt, 1982) and is composed of granodiorite that grades from weathered sediment to crystalline rock within the first few meters of the surface (Foster, 1976). Though seismic activity is frequent due to the proximity of the San Andreas and San Jacinto fault systems, local deformation rates are low. Numerous deployments over several decades indicate tilt rates $\ll 1 \mu$ rad/yr and strain rates $\ll 1 \mu$ strain/yr (Agnew, 2007; Wyatt et al., 1994), even during periods of high seismic activity (Agnew & Wyatt, 1989).

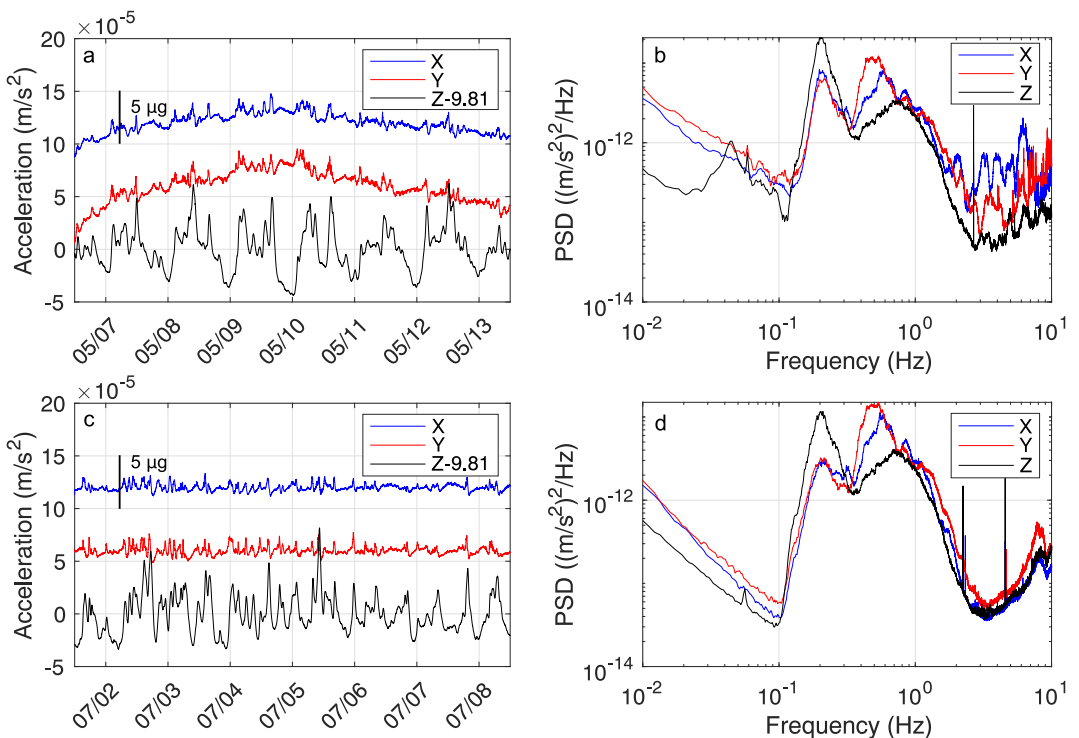


Figure 4. (a) Representative 6-day of data from Axial Seamount with the SCTA in the measurement orientation (with the Z-channel in the vertical) at Location 1 (before relocating the instrument) starting 05/06/2019 12:00 GMT. X-, Y-, and Z-channel observations are plotted in blue, red, and black, respectively, after removing the mean and linear trend and decimating to 1 sample/minute. Vertical offsets are for display purposes only. (b) Associated power spectral density for the three channels, calculated without decimating the data and plotted with the same colors. (c) Representative 6-day of data from Axial Seamount at Location 2 (after relocating the instrument) starting 7/01/2018 12:00 GMT, as in (a). (d) Associated power spectral density, as in (b).

The SCTA operated at PFO was the prototype of the seafloor version. The configuration of the gimbals, stepper motors, and brakes was identical to the instrument deployed at Axial Seamount, but it was attached to a square plate with three leveling feet and shielded by an acrylic housing (Figure 2e). We deployed the SCTA in a sealed vault several meters beneath the surface, on a concrete slab and enclosed under a box of rigid foam insulation. Within the vault there were large seasonal temperature variations of $>5^{\circ}\text{C}$ ($24.4\text{--}30.1^{\circ}\text{C}$) but shorter-period variations were much smaller (e.g., daily intervals have standard deviations of only $\sim 0.001^{\circ}\text{C}$).

Data were collected from 18 October 2018 to 16 January 2020 at 40 Hz, stored on a local drive, and uploaded daily to the University of Washington for archiving (Fredrickson et al., 2024). There were five data outages: one from February 14 to 28 March 2019 that was the result of a failure of the local computer (during this interval the instrument continued to run but no calibrations were performed), and shorter gaps from March 31 to 3 April 2019, April 27 to 29, 2019, 8 September 2019, and December 25 to 29, 2019 that were each the result of local power outages at the site. Figure S1 in Supporting Information S1 shows a representative week of data in time and frequency space while the SCTA was in measurement orientation. In this quiet setting, Earth tides are visible in the time domain. The spectrogram is dominated by the microseism peak and shows increased amplitudes above 1 Hz which is a result of frequency counting noise (Webb & Nooner, 2016). A peak at 6 and 7 Hz may be related to a mechanical resonance of the gimbals, which may differ from the Axial Seamount instrument due to small variations in construction between the two systems. A total of 32 calibrations were conducted at PFO (Table S3 in Supporting Information S1), of which the first 20 (prior to 9 August 2019) were 3-orientation sequences and the remaining 12 were five-orientation sequences.

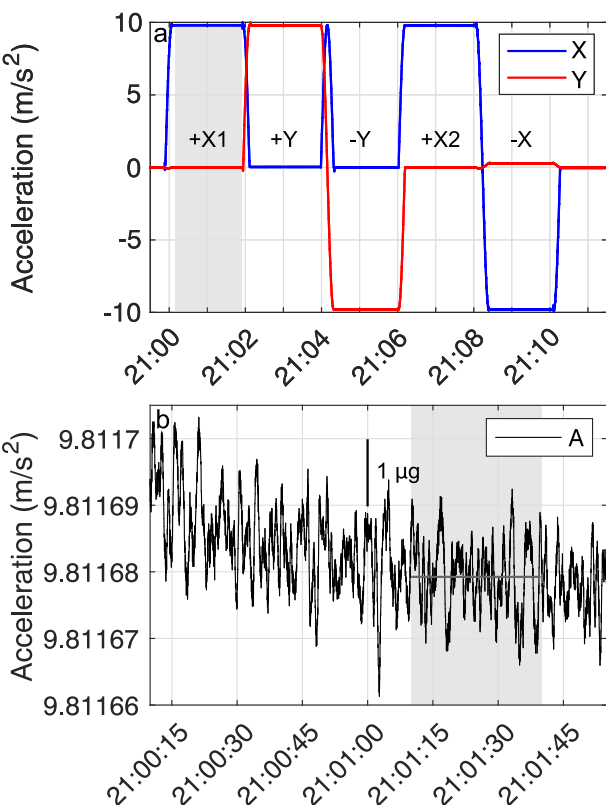


Figure 5. (a) X (blue) and Y channel (red) acceleration observations during a 5-orientation calibration sequence at Axial Seamount Location 2 on 10/15/2019, with calibration orientations labeled. Gray shaded area indicates the time interval plotted in (b). (b) Total acceleration observed during the interval indicated in (a), after the sensor has stabilized in the +X1 orientation and prior to beginning the next rotation. Gray shaded area indicates the interval over which the acceleration is averaged to get a calibration value. The dark gray horizontal line indicates the calculated calibration value during the interval.

the switch from the three-orientation to five-orientation sequence leads to a change in timing of the +X2 calibration relative to the onset of the sequence (Figure 1), so we solve for different values of b on either side of this change.

Table 1 gives the calibration values and model misfits for Axial Locations 1 and 2 while the model misfits for each calibration are plotted in Figures S2d and S2h in Supporting Information S1 (Location 1) and Figures 6d and 6h (Location 2). The drift for all channels at both locations is characterized by the fit to Equation 5 to better than 1 $\mu\text{g}/\text{yr}$. At Location 1, the span change over the period of five-orientation calibrations is $\sim 5 \mu\text{g}/\text{yr}$ for each channel, while at Location 2 the change in span for the X channel is $< 1 \mu\text{g}/\text{yr}$ and the change in span for the Y channel is $\sim 2.5 \mu\text{g}/\text{yr}$.

An example three-orientation calibration sequence from PFO is shown in Figure S6 in Supporting Information S1. The calibrations time series from PFO and Axial Seamount have initial transients with similar amplitudes, but the noise levels are much higher at Axial Seamount (compare Figure S6b in Supporting Information S1 and Figure 5b). The calibrations values from the PFO SCTA over the entire deployment are shown in Figure 7 and have a visually apparent temperature dependence and initial exponential transient. We account for temperature dependence by fitting the calibrations with an expression of the form

$$a_T^i(t) = b + ct + dT + e \frac{dT}{dt} + f \exp\left(\frac{-t}{h}\right) \quad (6)$$

4. Results

4.1. Calibrations Measurements

Figure 5a shows a representative five-orientation calibration sequence from Axial Seamount Location 2. There are noticeable short-term transients immediately following the change in orientation; the transients differ for each orientation and order in the calibration sequence but are repeatable from one sequence to the next. We define a single calibration value for each orientation in the sequence as the mean of the acceleration over a 30-s interval starting 60 s after the sensor has reached the calibration orientation (Figure 5b), thus excluding the interval immediately after the accelerometer has rotated, when the transients are largest. However, because the transients are repeatable, the measurements of drift (i.e., the sequential differences between calibrations) are not strongly sensitive to the interval selected, so long as that interval is kept consistent for all calibrations.

Calibrations for the full deployment period at Locations 1 and 2 are shown in Figure S2 in Supporting Information S1 and Figure 6, respectively. These plots exclude occasional anomalous calibrations that are scattered throughout the deployment at Axial Seamount. The cause of the anomalous calibrations is unknown, but they may be a result of an intermittent mechanical problem in the sensor. They are easily identified because the total acceleration a_T is inconsistent with that obtained at other times. They are discussed further in Text S1 in Supporting Information S1 and shown in Figures S3–S5 in Supporting Information S1.

To characterize the drift on each channel for each location, we fit a simple exponential-linear model (Polster et al., 2009; Watts & Kontoyiannis, 1990) to each set of calibrations of the form

$$a_T^i(t) = b + ct + f \exp\left(\frac{-t}{h}\right) \quad (5)$$

where superscript i indicates the sensor orientation and position in the calibration sequence (i.e., +X1, +Y, +X2, -X, -Y), t is time, and the terms b , c , f , and h are constants determined by a least squares inversion. For Location 1,

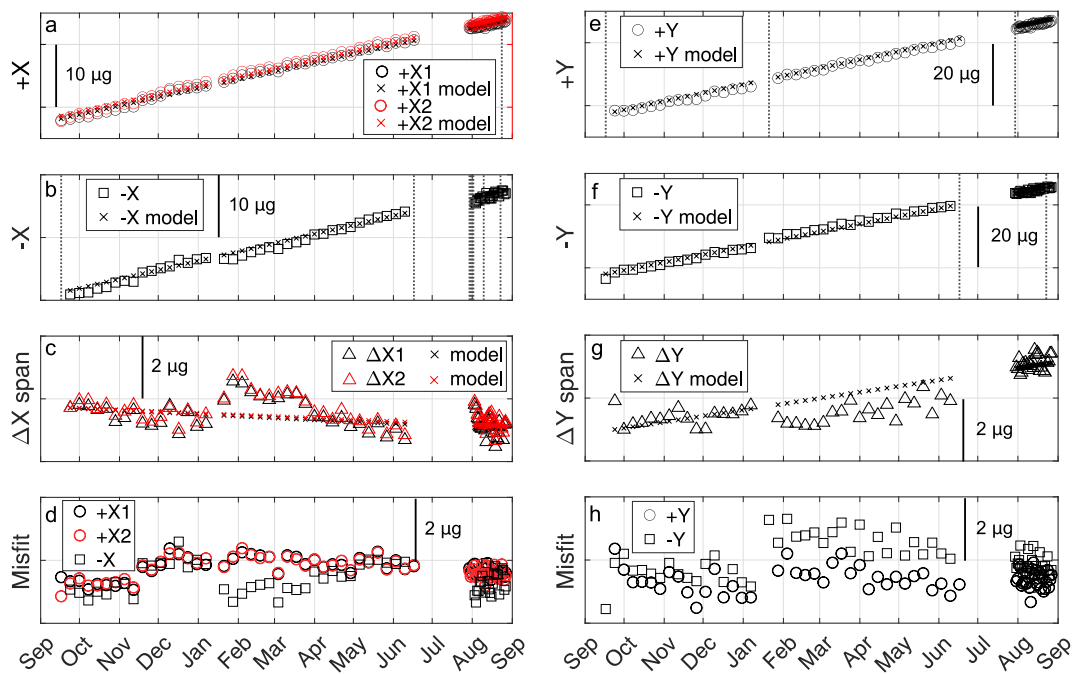


Figure 6. Calibration results and model values for the Axial Seamount SCTA at Location 2. (a) Calibration results for $+X_1$ (black) and $+X_2$ (red). (b) Calibrations results for $-X$. (c) X span results (defined as $+X$ minus $-X$). (d) Misfit of the exponential-linear model (Equation 5) for the $+X_1$, $+X_2$ and $-X$ calibrations. (e–h) As for (a–d) except for Y calibrations. Vertical dotted lines in (a) and (b) and (e) and (f) indicate where anomalous calibrations have been excluded (see text).

where T is temperature and d and e are additional constants obtained from the least squares inversion; we found that the temperature derivative term, with the derivative averaged over 1 day, was necessary to get a reasonable fit. As before, we allow b to have different value for the $+X_2$ calibrations on either side of the transition from 3- to 5-calibration sequences. We also found that the data were fit better with different values of b on either side of the 43-day interval of lost connectivity, likely because the instrument was disturbed thermally when the insulating cover was removed for inspection.

Figures 7d and 7h shows the model misfits after applying the model of Equation 6, and Table 1 lists the model parameters. The SCTA deployed at PFO was an entirely separate unit from that deployed at Axial and did not experience any anomalous calibrations. At PFO, the drift on each channel is characterized to $\sim 2 \mu\text{g}/\text{yr}$ (Table 1, Figures 7d and 7h) and the span change over the period of five-orientation calibrations is $< 3 \mu\text{g}/\text{yr}$ for each channel (Table 1, Figures 7c and 7g).

4.2. Applying Calibrations and Data Stitching

Generating a drift-corrected tilt time series involves applying a drift correction to each measurement segment, removing transient signals at the start of each segment, extrapolating the acceleration back to the end of the prior segment to account for the calibration interval, and applying a fixed offset to align the two segments at that time.

The drift for the X channel, s_X , at the time of the k th calibration, t_k , can be written for a three-orientation calibration sequence as

$$\sigma_X(t_k) = a_T^{+X}(t_k) - a_T^{+X}(t_1) \quad (7)$$

where the superscript $+X$ indicates the channel that is oriented vertically up, and drift is relative to the first calibration. For a five-orientation calibration sequence, a drift that accounts for changes in span can alternatively be written based on calibrations when vertically up ($+X$) and down ($-X$) as

Table 1

Calibration Model Parameters for Equations 5 and 6 and Misfit by Location and Orientation

		<i>b</i> – <i>g</i> (μg)	<i>c</i> ($\mu\text{g}/\text{yr}$)	<i>d</i> ($\mu\text{g}/\text{C}$)	<i>e</i> ($\mu\text{g}/(\text{C}/\text{d})$)	<i>f</i> (μg)	<i>h</i> (day)	RMS misfit (μg)
Axial Seamount Location 1	+X1	0.19	21.72	/	/	-26.50	2.40	0.37
	+X2	14.38	21.97	/	/	-24.50	2.07	0.36
		30.52 ^a						
	-X	-226.15	20.08	/	/	/	/	0.97
	X1 span	/	5.40 ^b	/	/	/	/	0.67 ^c
	X2 span	/	5.30 ^b	/	/	/	/	0.61 ^c
	+Y	-131.10	45.63	/	/	-30.40	1.22	0.75
	-Y	9.09	40.88	/	/	/	/	0.70
	Y span	/	5.15 ^b	/	/	/	/	0.44 ^c
Axial Seamount Location 2	+X1	42.17	16.61	/	/	/	/	0.30
	+X2	72.59	16.72	/	/	/	/	0.31
	-X	-247.24	17.34	/	/	/	/	0.44
	X1 span	/	-0.72 ^b	/	/	/	/	0.4 ^c
	X2 span	/	-0.68 ^b	/	/	/	/	0.39 ^c
	+Y	-28.54	31.86	/	/	/	/	0.36
	-Y	-44.05	29.60	/	/	/	/	0.58
	Y span	/	2.41 ^b	/	/	/	/	0.41 ^c
Piñon Flat Observatory	+X1	-2029.0	87.97	5.30	300.00	14.00	2.36	1.46
		-2034.56 ^d						
	+X2	-2008.98	86.87	5.30	300.00	13.80	2.28	2.01
		-2015.74 ^d						
		-1992.07 ^a						
	-X	-1769.32	81.40	5.30	300.00	/	/	2.27
	X1 span	/	-1.86 ^b	/	/	/	/	2.29 ^c
	X2 span	/	0.48 ^b	/	/	/	/	2.48 ^c
	+Y	-1986.68	100.38	8.44	260.00	14.90	4.53	1.01
		-1990.08 ^d						
	-Y	-1806.26	93.81	8.44	260.00	/	/	2.51
	Y span	/	3.43 ^b	/	/	/	/	1.7 ^c

^aFor these +X2 calibration this second value represents the value for *c* when the calibration switched from the 3-calibration to the 5-calibration sequence. ^bThe nominal span change (or drift) is not explicitly equal to the difference in drift between up and down directions, but rather the best linear fit to the difference between those calibrations. ^cFor the spans the misfit is based on a linear model to the difference of the up and down calibrations. ^dAt Piñon Flat Observatory, the constants for the 3-sequence calibration changed to these new values after the communication was restored following a laptop failure, likely because the sensor was disturbed when the insulating cover was temporarily removed for inspection.

$$\sigma_X(t_k) = \frac{\mathbf{a}_T^{+X}(t_k) + \mathbf{a}_T^{-X}(t_k)}{2} - \frac{\mathbf{a}_T^{+X}(t_1) + \mathbf{a}_T^{-X}(t_1)}{2} \quad (8)$$

To generate calibrated accelerations for the measurement interval between two calibrations, one can either subtract a linear interpolation between the drifts immediately preceding and following the measurement interval or subtract a smooth fit to the calibration data obtained by fitting a drift model such as those described in Equations 5 and 6. For the corrected data presented herein, we opt to use the definition of drift in Equation 7 and use the linear interpolation method.

Small gaps and offsets in the acceleration measurements result from rotating the SCTA to obtain calibrations. These are analogous to those seen for a bubble tiltmeter when it re-levels after going out of range (Agnew, 1986). For the SCTA they arise from a combination of periods of non-observation during calibrations, small changes in

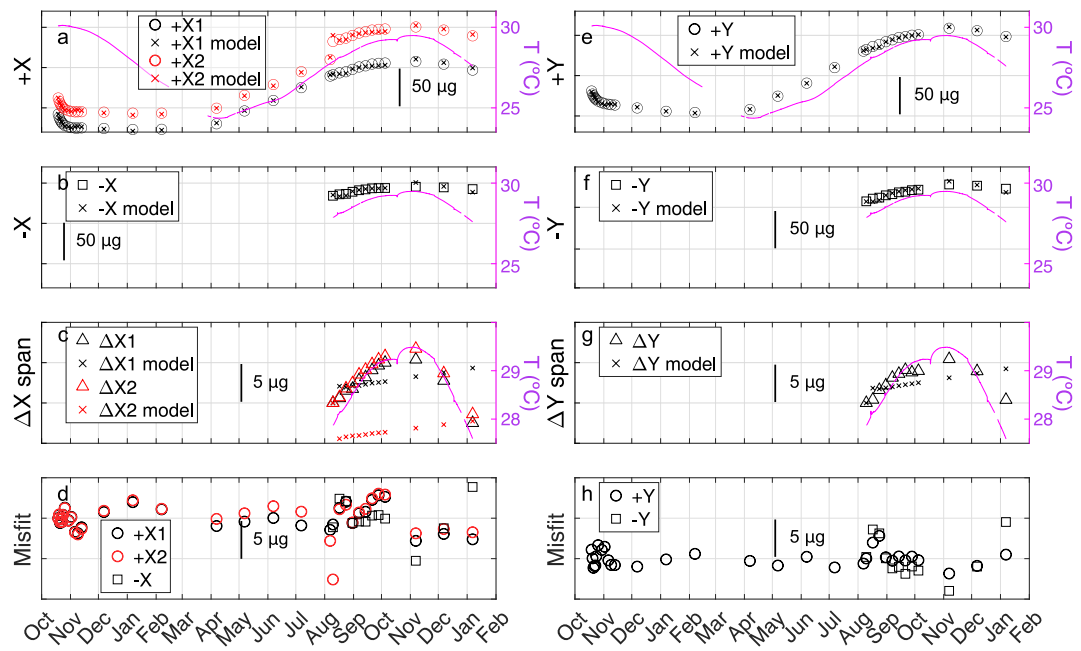


Figure 7. Calibration observations and model values, and temperatures for Piñon Flat Observatory. (a) Calibration results for $+X_1$ (black) and $+X_2$ (red) with temperature shown by purple on the righthand axis. (b) Calibrations results for $-X$. (c) Span results (defined as $+X$ minus $-X$). (d) Misfit of the exponential linear model with temperature terms (Equation 6) for the $+X_1$, $+X_2$, and $-X$ calibrations. (e–h) As for (a–d) except for Y calibrations.

orientation when the instrument is returned to the measurement orientation, and transients in the measured acceleration after rotation (analogous to those present in the calibration interval). To stitch the measurement intervals together, we must account for the transients at the start of each segment then extrapolate back in time to the end of the prior measurement interval. Mathematically, for the k th measurement interval, which we define as following the k th calibration, this can be written as

$$d'_{X,k}(t_{e,k-1}) = [a'_{X,k}(t_{s,k} + \delta t) - \delta a_X(\delta t)] \left(\frac{t_{e,k} - t_{e,k-1}}{t_{e,k} - t_{s,k} - \delta t} \right) - a'_{X,k}(t_{e,k}) \left(\frac{t_{s,k} + \delta t - t_{e,k-1}}{t_{e,k} - t_{s,k} - \delta t} \right) \quad (9)$$

where a' represents the linearly extrapolated acceleration, $t_{s,k}$ and $t_{e,k}$ are the start and end time of the k th measurement interval, respectively, δa_X is a time dependent transient referenced in time to the start of the measurement interval, and δt can be set to a non-zero value if the transient correction is unknown or has a large uncertainty immediately after the calibration. The correction represented by Equation 9 is demonstrated schematically in Figure 8.

At PFO, the data are sufficiently quiet and the transients sufficiently repeatable that they can be reliably modeled from an average of all such transients. Each individual transient is isolated from the surrounding data (which may not be static) by subtracting a linear trend calculated from the time series from 3 to 24 hr after the calibration. A mean transient is then calculated from the isolated individuals (Figure 9). The transient accelerations differ between the three- and five-orientation calibration sequences and the X and Y channels since they reflect a different history of orientations. The initial transient amplitudes are $\sim 20 \mu\text{g}$ but they decrease to absolute values of $\sim 1 \mu\text{g}$ within about an hour and to $\sim 0.1 \mu\text{g}$ after 5 hr (Figure 9). Over the entire interval, the standard deviation amongst the collection of transients is better than $0.25 \mu\text{g}$.

From the data at Axial Seamount, similar transient models can be calculated (Figure S7 in Supporting Information S1), which have comparable amplitudes to those at PFO, decaying from > 20 to $\sim 1 \mu\text{g}$ within an hour and to $\sim 0.1 \mu\text{g}$ within 5 hr. However, because of the elevated ambient noise in this setting, the averages are not as representative of the individual transients, with standard deviations approximately an order of magnitude larger than those seen at PFO (Figure S7 in Supporting Information S1).

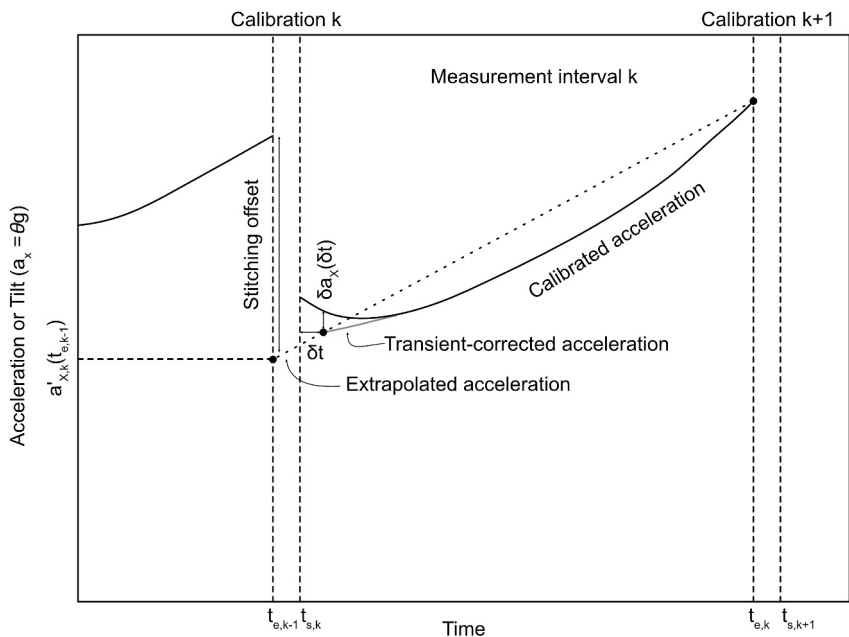


Figure 8. Demonstration of the stitching process with scale exaggerated for display purposes. There are three key components to stitching a continuous tilt time series: the tilt offset between data segments, the time offset between data segments (i.e., the calibration interval $t_{s,k} - t_{e,k-1}$) and the post-calibration transient ($\delta a_x(\delta t)$). Each data segment is corrected for its transient, extrapolated to time $t_{e,k-1}$, and then corrected for the tilt offset.

Equation 9 yields an extrapolated acceleration for the k th measurement interval, $a'_{X,k}(t_{e,k-1})$, at the end time of the previous ($k-1$ th) measurement interval. The $k-1$ th and k th measurement intervals can then be converted to tilt, corrected for drift, and stitched together simultaneously by calculating the end point tilts, q_X for each segment iteratively according to

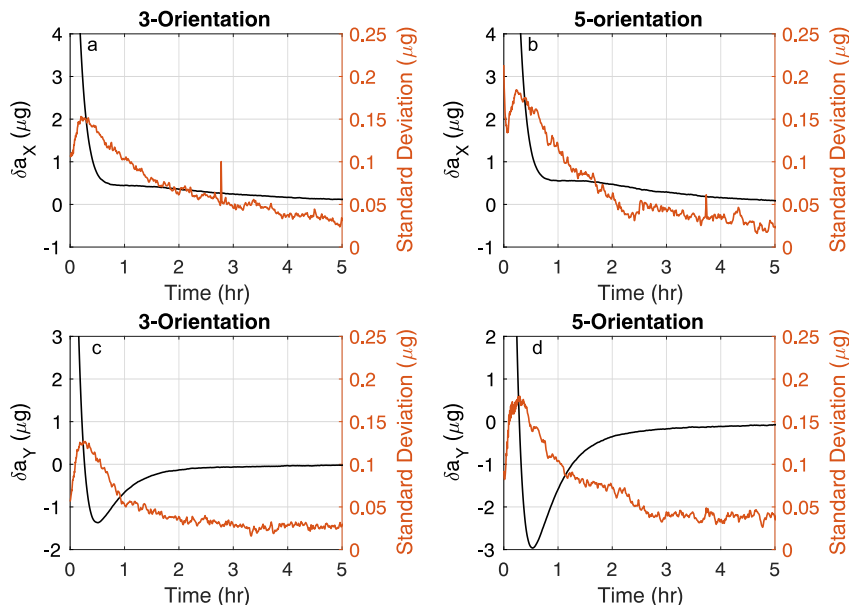


Figure 9. Transient accelerations (black lines) observed at PFO after the calibrations for (a) the X channel and the three-orientation sequence, (b) the X channel and the five-orientation sequence, (c) the Y channel and the three-orientation sequence and (d) the Y channel and the five-orientation sequence. The standard deviation (red lines) will be a combination of any variation in the post-calibration transient and variations in environmental noise between intervals.

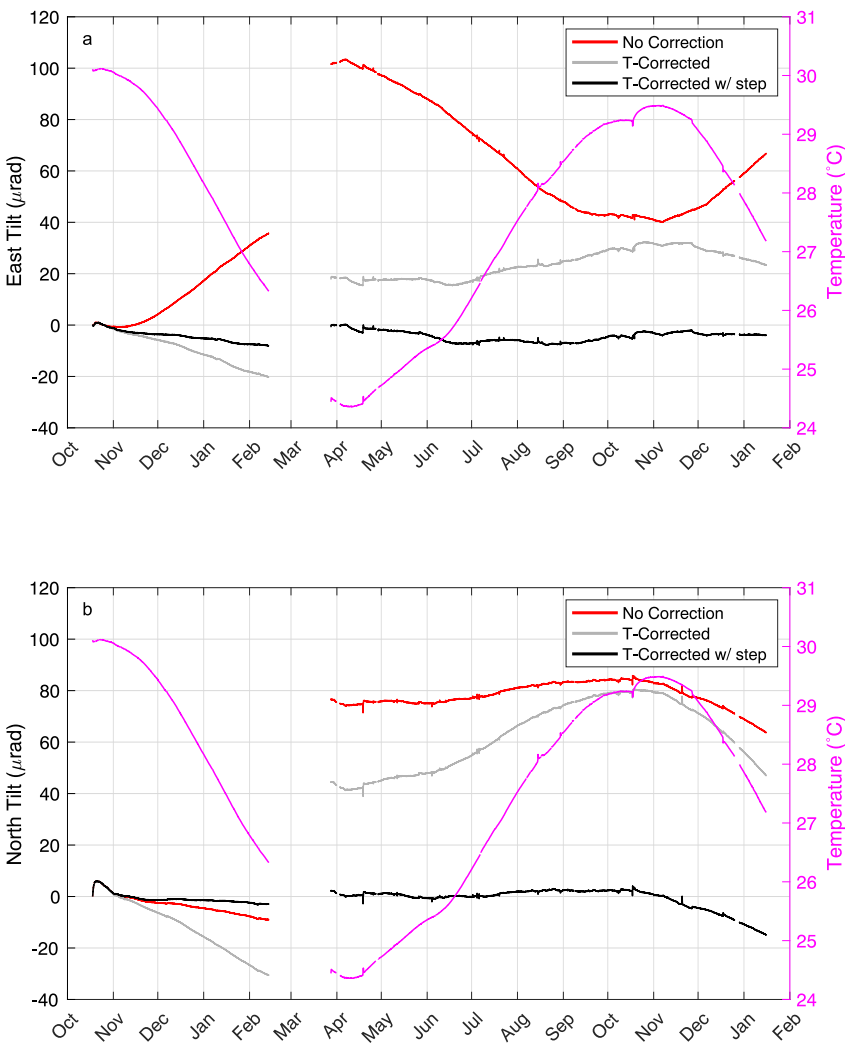


Figure 10. Time series of 1-min averaged tilt for Piñon Flat Observatory from 2018 to 2020 for the (a) east ($-Y$) and (b) north ($+X$) directions. The drift-corrected data, stitched with $dt = 5$ hr in Equation 9, are plotted in red. Stitched data are also shown after adjusting for linear temperature dependence (gray) and after adjusting for both the linear temperature dependence and a step at the 46-day gap (black). The temperature is plotted in purple. The sign convention is positive for a downward tilt.

$$\begin{aligned}\theta_X(t_{e,0}) &= 0 \\ \theta_X(t_{e,1}) &= \left[a_{X,1}(t_{e,1}) - a'_{X,1}(t_{e,0}) - \sigma_X(t_{e,1}) \right] / g \\ \theta_X(t_{e,k+1}) &= \theta_X(t_{e,k}) + \left[a_{X,k+1}(t_{e,k+1}) - a'_{X,k+1}(t_{e,k}) - \sigma_X(t_{e,k+1}) + \sigma_X(t_{e,k}) \right] / g\end{aligned}\quad (10)$$

In practice, we perform the calibration and stitching process on data that have been decimated by averaging to 1 sample/minute, which is more than sufficient for assessing the geodetic capabilities of the SCTA. Additionally, at Axial Seamount, the acceleration data are too noisy to perform stitching and extrapolation using single points at the start and end of each segment, so we instead used average values over the first and last 4 hr of each segment. The resulting stitched time series are not sensitive to this number so long as several hours or more are used.

4.3. Calibrated Tilt Observations at PFO and Axial Seamount

Figure 10 shows the results of stitching the data at PFO, converted to cardinal directions, following the standard convention of positive values representing tilt downward in that direction. Here the data have been stitched by

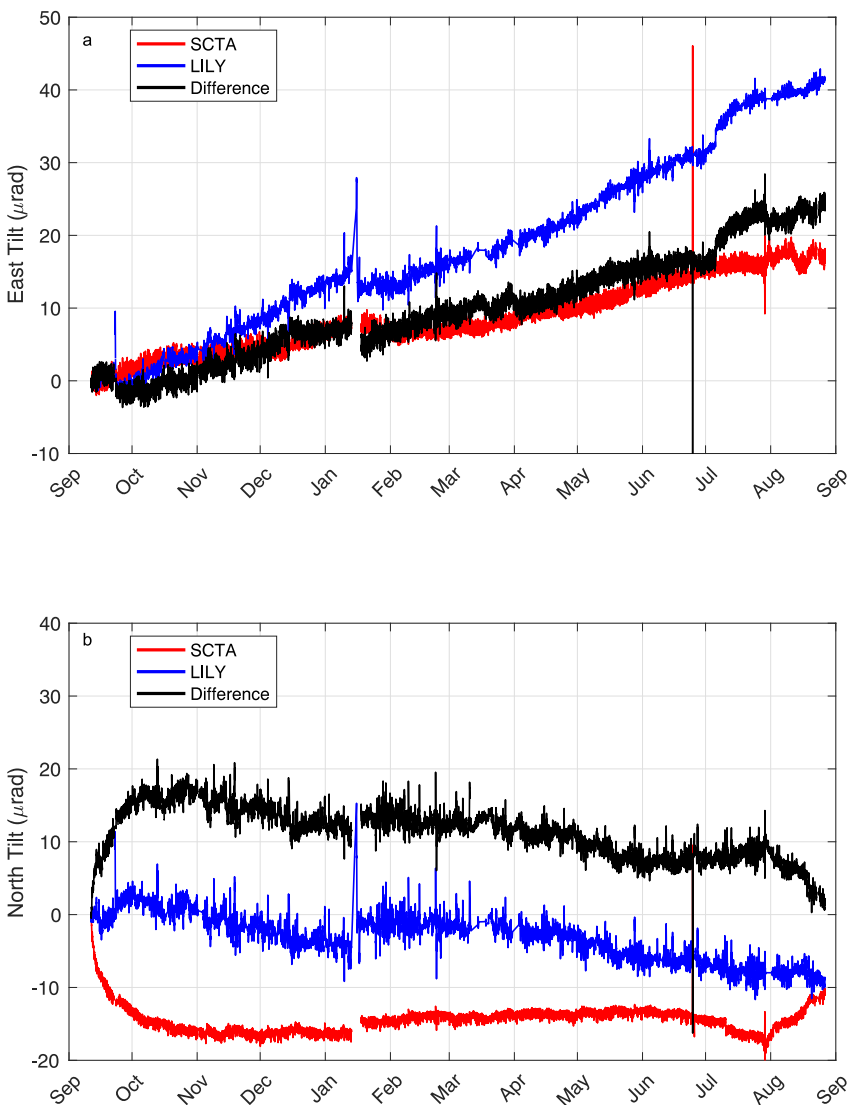


Figure 11. Time series of 1-min averaged tilt for Axial Seamount Location 2 from 2020 to 2021 for the (a) east and (b) north directions. Each panel shows the drift corrected SCTA data (red), stitched using $dt = 5$ hr in Equation 9, the LILY tilt meter data (blue) and the difference (LILY—SCTA) (black). The sign convention is positive for a downward tilt.

setting $dt = 5$ hr in Equation 9 to avoid a significant transient correction. Choosing to instead set $dt = 0$ hr and correcting with the composite average post-calibration transient leads to a ~ 1 μrad difference in the accumulated tilt over the experiment (Figure S8 in Supporting Information S1). The calibrated tilt time series shows a strong temperature dependence (red lines, Figure 10), particularly in the east tilt (parallel to Y channel). Since the temperature dependence of the accelerometer output should be removed by the calibrations, we infer that this may reflect thermal deformation of the SCTA apparatus. Solving for a least squares linear temperature correction that allows for a static offset after the data outage significantly flattens the tilt time series (black lines, in Figure 10) leaving residual signals that suggest < 10 μrad of tilt down to the west and ~ 15 μrad of tilt down to the south over the 16-month experiment.

At Axial Seamount, we stitch by setting $dt = 5$ hr in Equation 9 to minimize the impact of the poorly constrained transients. The results are shown along with the tilt data from the nearby LILY tiltmeter for Location one in the SCTA X-Y coordinates in Figure S9 in Supporting Information S1 and for Location 2 in geographic coordinates in Figure 11. At Location 1 (Figure S9 in Supporting Information S1), the results are not consistent with the LILY tiltmeter, and the difference suggests subsidence of the southeast leg of the SCTA platform. At Location 2, the

SCTA shows $\sim 25 \mu\text{rad}$ of downward tilt to the east over the year, while the LILY sensor indicates $\sim 40 \mu\text{rad}$ of downward tilt (Figure 11a). On the north channel the SCTA initially tilts to the north for about a month, possibly indicating platform settling. Following this there is very little net tilt while LILY shows about $10 \mu\text{rad}$ s of tilt down to the south.

5. Discussion

5.1. Calibration Technique

The calibration data collected at Axial Seamount (Figure 6 and Figure S5 in Supporting Information S1) and PFO (Figure 7) suggest that the rotational calibration approach is a valid method for measuring sensor drift. A small proportion of calibrations at Axial Seamount exhibit anomalous behavior for unknown reasons (see Text S1 in Supporting Information S1), but these anomalous calibrations are readily identifiable and therefore easily excluded. The remaining calibrations at Axial Seamount are well fit to RMS residuals of $\sim 0.5 \mu\text{g}$ (Table 1) using the exponential-linear functional form that is commonly used to characterize the drift of quartz sensors (Polster et al., 2009; Watts & Kontoyiannis, 1990). At PFO, where there were seasonal temperature variations of $>5^\circ\text{C}$, the calibration data are fit to RMS residuals of $\sim 2 \mu\text{g}$ (Table 1) when additional terms are added for linear dependence on temperature and the time derivative of temperature. The results show a linear sensor drift for the SCTA at Axial Seamount that is a few tens of $\mu\text{g}/\text{yr}$ (Table 1) on both channels and that decreases between Location 1 and Location 2, consistent with decreasing drift rates with sensor age. At PFO, the linear drift rates of $\sim 100 \mu\text{g}/\text{yr}$ are larger than Axial Seamount, likely because the accelerometer was newer.

Midway through the deployments at each site, we introduced a more complex, five-orientation calibration sequence that rotates each horizontal channel for calibrations pointing up and down. These measurements enable us to measure changes in the accelerometer span and thus correct for changes in both drift and sensitivity. For all the deployments, the rate of change of span is $\leq \sim 5 \mu\text{g}/\text{yr}$, which is approximately an order of magnitude lower than the drift rate in each case. We discuss this effect further in Section 5.2.

Each calibration sequence leads to a transient response lasting several hours that is very consistent, to $\leq \sim 0.1 \mu\text{g}/\text{yr}$ for a given channel and calibration sequence (Figure 9). This memory effect in the accelerometer output means that it is important to keep the calibration rotational sequence consistent in terms of order and timing and to make the calibration measurements over a consistent time interval after each rotation.

5.2. Axial Seamount Tilt Observations

The tilt data collected at Location 1 at Axial Seamount central caldera site (Figure S9 in Supporting Information S1) were impacted by settling of one leg of the tripod platform which was accidentally deployed on a layer of loose sediment. At Axial Seamount Location 2 (Figure 11), the calibrated and stitched east tilt observations show a downwards tilt of about $20 \mu\text{rad}/\text{yr}$, compared to a $\sim 40 \mu\text{rad}/\text{yr}$ eastward tilt recorded on the adjacent LILY tiltmeter over the same interval (Figure 11a). To the north, except for the first month, when there may be a post-relocation settling signal on the SCTA, the tilt observations are mostly stable to within $\sim 5 \mu\text{rad}/\text{yr}$, while the LILY tiltmeter shows $\sim 10 \mu\text{rad}/\text{yr}$ to the south (Figure 11b). In either direction, the calibrated SCTA tilt time series differs from the LILY observations by no more than $\sim 20 \mu\text{rad}/\text{yr}$. Kitada et al. (2013) conducted multiyear testing on LILY tiltmeters that demonstrated linear drift rates on these sensors as large as $\sim 70 \mu\text{rad}/\text{yr}$ even in deep, cemented borehole environments. Thus, though there is significant uncertainty in the LILY tiltmeter at Axial that exceeds the amplitude of its inferred tilt signal, within the bounds of this uncertainty the LILY tilt is not inconsistent with the drift-corrected SCTA data.

There have been various efforts to model the Axial volcano inflation source from bottom pressure observations (Hefner et al., 2020; Nooner & Chadwick, 2016), repeat mapping with an autonomous underwater vehicle (AUV) (Caress et al., 2020), or both (Slead et al., 2024). Though the system is underdetermined, the preferred model by Nooner and Chadwick (2016), based on the pressure data from the most recent eruption, places the center of inflation to the southeast of the central caldera site (Figure 3b). A subsequent model by Hefner et al. (2021) that accounted for slip on the caldera's ring faults placed the center of inflation to the southwest (Figure 3b). Slead et al. (2024) used both pressure and fly over altimetry data between 2015 and 2020 to constrain several models of ranging complexity, from simple 2-dimensional sill to distributed 3-dimensional variable inflation sources. These models predict inflation centers at variable locations relative to the central caldera site, all roughly at angles

from north through to southeast relative to the SCTA. The resultant tilt at the SCTA site from these models spans a wide range of azimuths, underscoring the uncertainty in the expected tilt signal at this site. Most of the predicted tilts are not strongly consistent with the SCTA, which records a largely eastward tilt in the Location 2 data, after the sensor was moved and settling issue resolved (red vector, Figure 3b). Likewise, the LILY tilt observations, which indicate an east-southeastern tilt, are also inconsistent with the models (blue vector, Figure 3b). “Model 3b” of Slead et al. (2024), which models the roof of the main magma chamber as a sill inflation source, shows the closest alignment with the SCTA and LILY tilt data, though it predicts a somewhat more southerly tilt (dotted white vector, Figure 3b). We note that, with the exception of “Model 1” from Slead et al. (2024), all of the modeled centers of inflation are very close to the central caldera site, indicating that small relocations can lead to dramatic changes inferred tilt direction. Even with a more definitive model, the deformation field at the central caldera is likely complex and heterogeneous, as suggested by the complex patterns of faulting seen in the seismicity (e.g., Zhang et al., 2024), and given that the caldera floor is composed of relatively poorly consolidated and fragmented material, which would promote localized block tilting (Arnulf et al., 2014; Baillard et al., 2019).

5.3. Piñon Flat Observatory Tilt Observations

The ongoing deformation of Axial Seamount limits our ability to assess the accuracy of the SCTA at that location because the true tilt signal is unknown. Conversely, at PFO, the expected tilt signal is << 1 µrad/yr (Agnew, 2007; Wyatt et al., 1994), making it a good site to assess the accuracy of SCTA. However, the large seasonal temperature variations observed within the vault impact the sensor and complicate this assessment. To fit the calibration data, it was necessary to include not only a temperature dependent term but also a term dependent on the time derivative of temperature, and the resulting exponential-linear drift model fits had an RMS about four times larger than were obtained for the SCTA at Axial. After applying the calibrations, the resulting stitched tilt records show a strong temperature dependence (red curves, Figure 10), even though this should theoretically be removed from the accelerometer by the calibrations. We infer from this temperature dependence that the SCTA apparatus deformed thermally. Correcting for this effect with a linear temperature-dependent term (black curves, Figure 10) and allowing for an unknown step during a 43-day period when connections were lost significantly flattens the stitched tilt time series (gray curves, Figure 10). For the east direction the tilt still varies by ~10 µrad over the 15-month deployment (Figure 10a). For the north direction, the tilt signal is much smaller except near the very start and near the end when there is ~15 µrad of apparent tilt to the south over 3 months (Figure 10b). This latter signal could indicate slip of the breaking mechanism, since the north direction corresponds to the X-axis, which is sensitive to slip on the outer gimbal on which there is more mechanical leverage.

5.4. Implications for Calibrated Absolute Pressure Instruments

In recent years, there has been growing interest in calibrated, “drift-free” seafloor pressure instruments, such as the Self-Calibrating Pressure Recorder (SCPR) of Sasagawa et al. (2016) and A-0-A (ambient-zero-ambient) systems (e.g., Wilcock et al., 2021). Such instruments operate on analogous principles as the SCTA, with the SCPR obtaining calibrations against a reference pressure close to ambient generated by a deadweight tester and the A-0-A obtaining calibrations against the atmospheric pressure inside the instrument housing. One of the potential sources of uncertainty in such systems is uncertainties in the reference pressure, whether from frictional effects in the deadweight tester or from drift in the barometer used to ground truth the internal pressure in the A-0-A, but such effects are generally assumed to be small. Another potential source of uncertainty in the A-0-A method is span change or drift in the sensor over the course of the deployment, which would result in calibrations at atmospheric pressure that are not fully representative of drift at high pressure. This change in span cannot be easily measured for pressure gauges but it can be measured for the SCTA when calibrations are obtained for each channel in both the up and down directions, as was done in the latter part of both our deployments. Since both the pressure gauges and accelerometers operate by measuring a changing load on a resonating quartz crystal, our results from the SCTA provides insights into the level of span change that might be expected in calibrated pressure instruments.

In total, our deployments yielded span sensitivity observations on four sensors: the X and Y channels at each location (Table 1). At Axial Seamount Location 1 on the X channel, we observed a ~5 µg/yr change in span, which is approximately 22% of the drift rate over the same period. On the Y channel, we also observed a ~5 µg/yr change in span, equal to ~12% of the drift rate on that channel. Interestingly, at Location 2 on the X channel, we observed only a ~0.7 µg/yr change in span, or 5% of the drift rate, while on the Y channel, we observed a ~2.4 µg/

yr change in span, or ~8% of the drift rate. These differences may suggest that whatever physical process disrupts the drift rate on these quartz crystals when instruments are redeployed may also be linked to the rate of span change. At PFO, residual temperature effects add uncertainty, but on the X channel, we observed a 1–2 $\mu\text{g}/\text{yr}$ change in span, equal to 1%–2% of the drift rate, and on the Y channel we observed a ~3.5 $\mu\text{g}/\text{yr}$ change, or ~4% of the drift rate. Thus, we see a range of span changes in these few sensors, from as little as 1% of the drift rate to as large as 22% of that rate. Given the commonalities between the SCTA and calibrated pressure systems in terms of their mechanical functionality, it is reasonable to assume that those instruments are likewise subject to variable rates of span change. Potentially, the SCTA could be used to further assess the span change for a larger number of quartz crystals and over longer durations to better constrain this source of uncertainty to A-0-A measurements.

6. Conclusions

Two deployments of our novel SCTA tiltmeter design, one at Piñon Flat Observatory and the other at Axial Seamount, show promising results for the rotational calibration method to correct instrumental drift, removing ~100 $\mu\text{rad}/\text{yr}$ and 15~40 $\mu\text{rad}/\text{yr}$ drifts, respectively. However, due to complications at each site, neither provides a well-constrained test of the accuracy of resulting tilt time series. At Axial Seamount, the true signal of the inflating caldera is unknown while at Piñon Flat Observatory, large seasonal temperature variations impact the data. Further, the large number of calibrations performed in these initial tests exacerbated the challenges associated with stitching the tilt time series together. The SCTA would benefit from a long deployment in a tectonically stable setting with much smaller temperature fluctuations than the vault at Piñon Flat Observatory. This could be accomplished by deployment at moderate depths in a borehole where the temperature fluctuations are expected to be several orders of magnitude smaller than observed in the vault at Piñon Flat Observatory vault (e.g., Kinoshita et al., 2009). Such further investigations would not only reveal the capabilities and limitations of the SCTA as a geodetic sensor, but would also provide useful information for analogous A-0-A pressure instruments, for which absolute drift and span change cannot be as easily constrained.

Data Availability Statement

For the SCTA at Axial Seamount, unprocessed acceleration and temperature data are available on EarthScope Consortium Web Services under Network “OO,” Station “AXCC2” (Rutgers University, 2013). For the SCTA at PFO, unprocessed acceleration and temperature data are available on Dryad (Fredrickson et al., 2024).

Acknowledgments

We thank the OOI RCA field team, the ROV *Jason* and the captains and crews of the *R/V Roger Revelle* and *R/V Thomas G. Thompson* for deploying and recovering the Axial Seamount SCTA, Bill Chadwick and colleagues for providing the opportunity to move the Axial Seamount SCTA during a *R/V Thomas G. Thompson* and ROV *Jason* cruise, and Mark Zumberge and Glenn Sasagawa for providing space in the vault, internet connectivity and field assistance for the test at Piñon Flat Observatory. We also thank the editor, Kristy Tiampo, and two anonymous reviewers for their helpful input. This work was supported by National Science Foundation OCE Grant 1634103.

References

- Agnew, D. C. (1986). Strainmeters and tiltmeters. *Reviews of Geophysics*, 24(3), 579–624. <https://doi.org/10.1029/RG024i003p00579>
- Agnew, D. C. (2007). Before PBO: An overview of continuous strain and tilt measurements in the United States. *Journal of the Geodetic Society of Japan*, 53(2), 157–182.
- Agnew, D. C., & Wyatt, F. K. (1989). The 1987 Superstition Hills earthquake sequence: Strains and tilts at Piñon Flat Observatory. *Bulletin of the Seismological Society of America*, 79(2), 480–492. <https://doi.org/10.1785/BSSA0790020480>
- Anderson, G., Constable, S., Staudigel, H., Wyatt, F. K., Et, A., & Seafloor, A. L. (1997). A seafloor longbaseline tiltmeter inflation of Axial Seamount to be below. *Geophysics*, 102(B9), 20269–20285. <https://doi.org/10.1029/97jb01586>
- Araki, E., Kimura, T., Machida, Y., Yokobiki, T., Nishida, S., Kawaguchi, K., et al. (2017). Deep seafloor borehole observatories for seismogenic zone monitoring. *Techno-Ocean 2016: Return to the Oceans*, 332, 656–659. <https://doi.org/10.1109/Techno-Ocean.2016.7890737>
- Arnulf, A. F., Harding, A. J., Kent, G. M., Carbotte, S. M., Canales, J. P., & Nedimović, M. R. (2014). Anatomy of an active submarine volcano. *Geology*, 42(8), 655–658. <https://doi.org/10.1130/G35629.1>
- Baillard, C., Wilcock, W. S. D., Arnulf, A. F., Tolstoy, M., & Waldhauser, F. (2019). A joint inversion for three-dimensional P and S wave velocity structure and earthquake locations beneath axial seamount. *Journal of Geophysical Research: Solid Earth*, 124(12), 12997–13020. <https://doi.org/10.1029/2019JB017970>
- Bevis, M., Kendrick, E., Smalley, R., Brooks, B., Allmendinger, R., & Isacks, B. (2001). On the strength of interplate coupling and the rate of back arc convergence in the central Andes: An analysis of the interseismic velocity field. *Geochemistry, Geophysics, Geosystems*, 2(11), 1067. <https://doi.org/10.1029/2001GC000198>
- Bock, Y., Agnew, D. C., Fang, P., Genrich, J. F., Hager, B. H., Herring, T. A., et al. (1993). Detection of crustal deformation from the Landers earthquake sequence using continuous geodetic measurements. *Nature*, 361(6410), 337–340. <https://doi.org/10.1038/361337a0>
- Bürgmann, R., & Chadwell, D. (2014). Seafloor geodesy. *Annual Review of Earth and Planetary Sciences*, 42(May), 509–534. <https://doi.org/10.1146/annurev-earth-060313-054953>
- Bürgmann, R., & Thatcher, W. (2013). Space geodesy: A revolution in crustal deformation measurements of tectonic processes. In *The Web of geological sciences: Advances, impacts, and interactions*. Geological Society of America. [https://doi.org/10.1130/2013.2500\(12\)](https://doi.org/10.1130/2013.2500(12))
- Carbotte, S. M., Arnulf, A., Spiegelman, M., Lee, M., Harding, A., Kent, G., et al. (2020). Stacked sills forming a deep melt-mush feeder conduit beneath axial seamount. *Geology*, 48(7), 693–697. <https://doi.org/10.1130/G47223.1>
- Caress, D. W., Clague, D. A., Paduan, J. B., Chadwick, W. W., Noonan, S. L., & Thomas, H. J. (2020). Vertical deformation of the axial seamount summit from repeated 1-m scale bathymetry surveys using AUVs. In *AGU Fall Meeting Abstracts* (Vol. 2020, p. V040-0017).

- Chadwick, W. W., Nooner, S. L., Butterfield, D. A., & Lilley, M. D. (2012). Seafloor deformation and forecasts of the April 2011 eruption at axial seamount. *Nature Geoscience*, 5(7), 474–477. <https://doi.org/10.1038/ngeo1464>
- Chadwick, W. W., Nooner, S. L., Zumberge, M. A., Embley, R. W., & Fox, C. G. (2006). Vertical deformation monitoring at Axial Seamount since its 1998 eruption using deep-sea pressure sensors. *Journal of Volcanology and Geothermal Research*, 150(1–3), 313–327. <https://doi.org/10.1016/j.jvolgeores.2005.07.006>
- Chadwick, W. W., Wilcock, W. S. D., Nooner, S. L., Beeson, J. W., Sawyer, A. M., & Lau, T. K. (2022). Geodetic monitoring at axial seamount since its 2015 eruption reveals a waning magma supply and tightly linked rates of deformation and seismicity. *Geochemistry, Geophysics, Geosystems*, 23(1). <https://doi.org/10.1029/2021GC010153>
- Chawah, P., Chéry, J., Boudin, F., Cattoen, M., Seat, H. C., Plantier, G., et al. (2015). A simple pendulum borehole tiltmeter based on a triaxial optical-fibre displacement sensor. *Geophysical Journal International*, 203(2), 1026–1038. <https://doi.org/10.1093/gji/ggv358>
- Davis, E., Krug, R., Debastiani, D., Oliveira, C., Pereira, L. C., & Rachid de Araujo, M. A. (2023). High precision seabed deformation monitoring. Day 1 Mon, May 01, 2023. <https://doi.org/10.4043/32207-MS>
- Duennebier, F. K., Cessaro, R. K., & Harris, D. (1987). Temperature and tilt variation measured for 64 days in hole 581C. In *Initial Reports of the Deep Sea Drilling Project* (Vol. 88, pp. 161–166).
- Dvorak, J. J., & Dzurisin, D. (1997). Volcano geodesy: The search for magma reservoirs and the formation of eruptive vents. *Reviews of Geophysics*, 35(3), 343–384. <https://doi.org/10.1029/97RG00070>
- Esmaili, S., Talebi, M., Pourdeilami, A., & Farsangi, E. N. (2023). Innovative cost-effective pendulum tiltmeter based on the moiré technique. *Optical Engineering*, 62(05). <https://doi.org/10.1117/1.OE.62.5.054101>
- Fabian, M., & Villinger, H. (2007). The Bremen ocean bottom tiltmeter (OBT)—A technical article on a new instrument to monitor deep sea floor deformation and seismicity level. *Marine Geophysical Researches*, 28(1), 13–26. <https://doi.org/10.1007/s11001-006-9011-4>
- Fabian, M., & Villinger, H. (2008). Long-term tilt and acceleration data from the Logatchev hydrothermal vent field, mid-Atlantic ridge, measured by the Bremen Ocean bottom tiltmeter. *Geochemistry, Geophysics, Geosystems*, 9(7), 1–12. <https://doi.org/10.1029/2007GC001917>
- Feigl, K. L., Agnew, D. C., Bock, Y., Dong, D., Donnellan, A., Hager, B. H., et al. (1993). Space geodetic measurement of crustal deformation in central and southern California, 1984–1992. *Journal of Geophysical Research*, 98(B12), 1984–1992. <https://doi.org/10.1029/93jb02405>
- Foster, J. (1976). Geology. In I. P. Ting & W. Jennings (Eds.), *Deep canyon, a Desert wilderness for science* (pp. 90–91). University of California.
- Fox, C. G. (1993). Five years of ground deformation monitoring on axial seamount using a bottom pressure recorder. *Geophysical Research Letters*, 20(17), 1859–1862. <https://doi.org/10.1029/93GL01216>
- Fredrickson, E. K., Wilcock, W. S. D., Baillard, C., Harrington, M., Cram, G., Tilley, J., et al. (2019). Observing and interpreting seafloor tilt at Axial Seamount. In *AGU Fall Meeting Abstracts* (Vol. 2019, p. OS51B-1490).
- Fredrickson, E. K., Wilcock, W. S. D., Harrington, M. J., Cram, G., Tilley, J., Martin, D., & Burnett, J. (2024). Data from: The self-calibrating tilt accelerometer: A method for observing tilt and correcting drift with a triaxial accelerometer [Dataset]. Dryad. <https://doi.org/10.5061/dryad.34tmpg4td>
- Furst, S., Chéry, J., Mohammadi, B., & Peyret, M. (2019). Joint estimation of tiltmeter drift and volume variation during reservoir monitoring. *Journal of Geodesy*, 93(8), 1137–1146. <https://doi.org/10.1007/s00190-019-01231-3>
- Gravirov, V. V., Deschcherevskii, A. V., Kuzmin, Y. O., Likhodeev, D. V., Sobisevich, A. L., & Shirokov, I. A. (2022). Improvements in high-precision tiltmeter instrument systems located in an underground geophysical observatory. *Seismic Instruments*, 58(4), 363–378. <https://doi.org/10.3103/S0747923922040041>
- Hefner, W. L., Nooner, S. L., Chadwick, W. W., & Bohnenstiehl, D. W. R. (2020). Revised magmatic source models for the 2015 eruption at axial seamount including estimates of fault-induced deformation. *Journal of Geophysical Research: Solid Earth*, 125(4), 1–11. <https://doi.org/10.1029/2020JB019356>
- Hefner, W. L., Nooner, S. L., Chadwick, W. W., Caress, D. W., Paduan, J. B., Bohnenstiehl, D. W. R., & Clague, D. A. (2021). Deformation models for the 2015-eruption and post-eruption inflation at Axial Seamount from repeat AUV bathymetry. In *AGU Fall Meeting Abstracts* (Vol. 2021, p. V45B-0138).
- Hensch, M., Dahm, T., Hort, M., Huebscher, C., & Dehghani, A. (2009). *On the interrelation of fluid-induced seismicity and crustal deformation at Columbo Seamount (Aegean Sea, Greece)*. University of Hamburg.
- Jahr, T., Jentzsch, G., & Weise, A. (2009). Natural and man-made induced hydrological signals, detected by high resolution tilt observations at the Geodynamic Observatory Moxa/Germany. *Journal of Geodynamics*, 48(3–5), 126–131. <https://doi.org/10.1016/j.jog.2009.09.011>
- Jahr, T., Letz, H., & Jentzsch, G. (2006). Monitoring fluid induced deformation of the Earth's crust: A large scale experiment at the KTB location/Germany. *Journal of Geodynamics*, 41(1–3), 190–197. <https://doi.org/10.1016/j.jog.2005.08.003>
- Kidiwela, M., Manalang, D., Wilcock, S. D., & Ploskey, J. (2023). An acoustic array at axial seamount for geodesy and autonomous vehicle support. In *From AGU Fall Meeting Abstracts* (Vol. 2023, p. G42-06).
- Kimura, T., Araki, E., & Kitada, K. (2013). Evaluation tests on tiltmeter and seismometer for the long-term borehole monitoring system. In *Proceedings of the 11th SEGJ International Symposium, Yokohama, Japan, 18–21 November 2013* (pp. 438–442). Society of Exploration Geophysicists. <https://doi.org/10.1190/segi112013-111>
- Kinoshita, M., Sayanagi, K., Kasaya, T., Araki, E., & Ito, H. (2009). Long-term temperatures measurements at some onland and sub-seafloor boreholes. In *JAMSTEC-R IFREE Special Issue, (November)* (pp. 21–25).
- Kitada, K., Araki, E., Kimura, T., Kinoshita, M., Kopf, A., & Saffer, D. (2013). Long-term monitoring at C0002 seafloor borehole in Nankai Trough seismogenic zone. In *2013 IEEE International Underwater Technology Symposium, UT 2013* (pp. 15–17). <https://doi.org/10.1109/UT.2013.6519882>
- Kreemer, C., Blewitt, G., & Klein, E. C. (2014). A geodetic plate motion and global strain rate model. *Geochemistry, Geophysics, Geosystems*, 15(10), 3849–3889. <https://doi.org/10.1002/2014GC005407>
- Liu, H.-F., Luo, Z.-C., Hu, Z.-K., Yang, S.-Q., Tu, L.-C., Zhou, Z.-B., & Kraft, M. (2022). A review of high-performance MEMS sensors for resource exploration and geophysical applications. *Petroleum Science*, 19(6), 2631–2648. <https://doi.org/10.1016/j.petsci.2022.06.005>
- Massonnet, D., Rossi, M., Carmona, C., Adragna, F., Peltzer, G., Feigl, K., & Rabauta, T. (1993). The displacement field of the Landers earthquake mapped by radar interferometry. *Nature*, 364(6433), 138–142. <https://doi.org/10.1038/364138a0>
- McCaffrey, R., King, R. W., Payne, S. J., & Lancaster, M. (2013). Active tectonics of northwestern U.S. inferred from GPS-derived surface velocities. *Journal of Geophysical Research: Solid Earth*, 118(2), 709–723. <https://doi.org/10.1029/2012JB009473>
- McGuire, J. J., Collins, J. A., Davis, E., Becker, K., & Heesemann, M. (2018). A lack of dynamic triggering of slow slip and tremor indicates that the shallow Cascadia megathrust offshore Vancouver Island is likely Locked. *Geophysical Research Letters*, 45(20), 11095–11103. <https://doi.org/10.1029/2018GL079519>
- Nooner, S. L., & Chadwick, W. W. (2009). Volcanic inflation measured in the caldera of Axial Seamount: Implications for magma supply and future eruptions. *Geochemistry, Geophysics, Geosystems*, 10(2). <https://doi.org/10.1029/2008GC002315>

- Nooner, S. L., & Chadwick, W. W. (2016). Inflation-predictable behavior and co-eruption deformation at Axial Seamount. *Science*, 354(6318), 1399–1403. <https://doi.org/10.1126/science.aah4666>
- Party, S. S. (2000). Borehole instrument package. In I. S. Sacks, K. Suyehiro, G. D. Acton, & E. Al (Eds.), *Proceedings of the Ocean Drilling Program, 186 Initial Reports* (Vol. 186). <https://doi.org/10.2973/odp.proc.ir.186.103.2000>
- Poland, M. P., & Zebker, H. A. (2022). Volcano geodesy using InSAR in 2020: The past and next decades. *Bulletin of Volcanology*, 84(3), 27. <https://doi.org/10.1007/s00445-022-01531-1>
- Polster, A., Fabian, M., & Villinger, H. (2009). Effective resolution and drift of paroscientific pressure sensors derived from long-term seafloor measurements. *Geochemistry, Geophysics, Geosystems*, 10(8). <https://doi.org/10.1029/2009GC002532>
- Rutgers University. (2013). Ocean observatories initiative [Dataset]. International Federation of Digital Seismograph Networks. <https://doi.org/10.7914/SN/OO>
- Sakata, S., & Shimada, S. (1984). Development of the Ocean bottom tiltmeter (2). *Journal of the Geodetic Society of Japan*, 30(1), 50–58. <https://doi.org/10.11366/sokuchi1954.30.50>
- Sasagawa, G., Cook, M. J., & Zumberge, M. A. (2016). Drift-corrected seafloor pressure observations of vertical deformation at Axial Seamount 2013–2014. *Earth and Space Science*, 3(9), 381–385. <https://doi.org/10.1002/2016EA000190>
- Shimamura, H., & Kanazawa, T. (1988). Ocean bottom tiltmeter with acoustic data retrieval system implanted by a submersible. *Marine Geophysical Researches*, 9(3), 237–254. <https://doi.org/10.1007/BF00309975>
- Shiobara, H., Ito, A., Sugioka, H., Shinohara, M., & Sato, T. (2021). Tilt observations at the seafloor by mobile ocean bottom seismometers. *Frontiers in Earth Science*, 8, 1–13. <https://doi.org/10.3389/feart.2020.599810>
- Slead, S. R., Wei, M., Nooner, S. L., Chadwick, W. W., Caress, D. W., & Beeson, J. (2024). Compartmentalization of axial seamount's magma reservoir inferred by analytical and numerical deformation modeling with realistic geometry. *Journal of Geophysical Research: Solid Earth*, 129(5). <https://doi.org/10.1029/2023JB028414>
- Takamori, A., Bertolini, A., Desalvo, R., Araya, A., Kanazawa, T., & Shinohara, M. (2011). Novel compact tiltmeter for ocean bottom and other frontier observations. *Measurement Science and Technology*, 22(11), 115901. <https://doi.org/10.1088/0957-0233/22/11/115901>
- Tolstoy, M., Constable, S., Orcutt, J., Staudigel, H., Wyatt, F. K., & Anderson, G. (1998). Short and long baseline tiltmeter measurements on axial seamount, Juan de Fuca Ridge. *Physics of the Earth and Planetary Interiors*, 108(2), 129–141. [https://doi.org/10.1016/S0031-9201\(98\)00091-0](https://doi.org/10.1016/S0031-9201(98)00091-0)
- Tsuji, S., Araki, E., Yokobiki, T., Nishida, S., Machida, Y., Zumberge, M., & Takahashi, K. (2023). Precise tilt measurement by seafloor borehole tiltmeters at the Nankai Trough subduction zone. *Earth Planets and Space*, 75(1), 188. <https://doi.org/10.1186/s40623-023-01946-w>
- Watts, D. R., & Kontoyiannis, H. (1990). Deep-ocean bottom pressure measurement: Drift removal and performance. *Journal of Atmospheric and Oceanic Technology*, 7(2), 296–306. [https://doi.org/10.1175/1520-0426\(1990\)007<0296:dobpmid>2.0.co;2](https://doi.org/10.1175/1520-0426(1990)007<0296:dobpmid>2.0.co;2)
- Webb, S. C., & Nooner, S. L. (2016). High-resolution seafloor absolute pressure gauge measurements using a better counting method. *Journal of Atmospheric and Oceanic Technology*, 33(9), 1859–1874. <https://doi.org/10.1175/JTECH-D-15-0114.1>
- Wilcock, W. S. D., Manalang, D. A., Fredrickson, E. K., Harrington, M. J., Cram, G., Tilley, J., et al. (2021). A thirty-month seafloor test of the A-O-A method for calibrating pressure gauges. *Frontiers in Earth Science*, 8. <https://doi.org/10.3389/feart.2020.600671>
- Wilcock, W. S. D., Tolstoy, M., Waldhauser, F., Garcia, C., Tan, Y. J., Bohnenstiehl, D. R., et al. (2016). Seismic constraints on caldera dynamics from the 2015 Axial Seamount eruption. *Science*, 354(6318), 1395–1399. <https://doi.org/10.1126/science.aah5563>
- Wyatt, F. (1982). Displacement of surface monuments: Horizontal motion. *Journal of Geophysical Research*, 87(B2), 979–989. <https://doi.org/10.1029/JB087B02p00979>
- Wyatt, F. K., Agnew, D. C., & Gladwin, M. (1994). Continuous measurements of crustal deformation for the 1992 Landers earthquake sequence. *Bulletin of the Seismological Society of America*, 84(3), 768–779. [https://doi.org/10.1016/0148-9062\(95\)94488-5](https://doi.org/10.1016/0148-9062(95)94488-5)
- Yang, J., Zhu, H., Zhao, Z., Huang, J., Lumley, D., Stern, R. J., et al. (2024). Asymmetric magma plumbing system beneath Axial Seamount based on full waveform inversion of seismic data. *Nature Communications*, 15(1), 4767. <https://doi.org/10.1038/s41467-024-49188-y>
- Zhang, M., Wilcock, W. S. D., Waldhauser, F., Wang, K., Schaff, D., Tolstoy, M., & Tan, Y. (2024). A catalog of automated focal mechanisms for microearthquakes at axial seamount based on waveform cross-correlation. In *SSA Annual Meeting Abstracts* (2024).
- Zumberge, M., Berger, J., Hatfield, W., & Wielandt, E. (2018). A three-component borehole optical seismic and geodetic sensor. *Bulletin of the Seismological Society of America*, 108(4), 2022–2031. <https://doi.org/10.1785/0120180045>